On the Formation of Phantom Electron Phase Space Density Peaks in Single Spacecraft Radiation Belt Data

L. Olifer[1], I. R. Mann[1], L. G. Ozeke[1], S. K. Morley[2], H. L. Louis[1]

[1]Department of Physics, University of Alberta, Edmonton, AB, Canada

[2]Space Science and Applications, Los Alamos National Laboratory, Los Alamos, NM, USA

Key Points:

- GPS electron flux data reveal fast magnetopause shadowing radiation belt losses during the September 2017 geomagnetic storm
- A single subsequent apparent local peak in electron phase space density is observed during storm recovery, suggestive of local acceleration
- Fortuitous timing and L-shell coverage from the two Van Allen Probes instead reveals the source as very fast inward radial diffusion

Corresponding author: Leonid Olifer, `olifer@ualberta.ca`

Abstract

This paper examines the rapid losses and acceleration of trapped relativistic and ultra-relativistic electron populations in the Van Allen radiation belt during the September 7-9, 2017, geomagnetic storm. By analyzing the dynamics of the last closed drift shell (LCDS) and the electron flux and phase space density (PSD), we show that the electron dropouts are consistent with magnetopause shadowing and outward radial diffusion to the compressed LCDS. During the recovery phase, an in-bound pass of Van Allen Probe A shows an apparent local peak in PSD. However, a fortuitous timing of a crossing of the two Van Allen Probes reveals instead how the apparent PSD peak arises from aliasing monotonic PSD profiles which are rapidly increasing due to acceleration from very fast inwards radial diffusion. In the absence of such multi-satellite conjunctions during fast acceleration events, the source might otherwise be attributed to local acceleration processes.

Plain Language Summary

This paper presents a thorough analysis of terrestrially trapped electron space radiation during the September 2017 geomagnetic storm. By analyzing the measurements of the trapped electron population, we show that the predominant loss of the relativistic and ultra-relativistic electrons depleted from the radiation belt at the beginning of the storm arises from outwards loss into the solar wind and not downwards loss into the atmosphere. We also reveal for the first time that the signatures of the acceleration processes which refill the belts after such losses can occur on much faster timescales than previously thought. Moreover, signatures attributed to the actions of high-frequency plasma waves, are actually caused by a different physical phenomenon known as radial diffusion. The new knowledge of the very fast rate of change of the amount of electron space radiation points to an urgent need to evaluate the processes which control belt dynamics. As we show here, this can be faster than the orbital period of monitoring satellites. Overall, we show how the limited satellite spatio-temporal coverage may mask and confuse the signatures of the physical processes responsible.

1 Introduction

Since the discovery of the terrestrially trapped electron radiation in the Van Allen radiation belts (Van Allen & Frank, 1959), understanding the processes which govern

belt dynamics has remained an active area of research (see e.g., the review by Millan & Thorne, 2007, and references therein). A lot of attention has been dedicated to examining the underlying physics of the plasma wave-particle interactions inside the Earth's magnetosphere in pursuit of developing accurate simulation models and potentially predicting Van Allen belt behavior (e.g., Shprits, Elkington, et al., 2008; Shprits, Subbotin, et al., 2008). The processes that cause particle loss and acceleration are those which attract the most attention since in combination they can cause the radiation belt to change drastically on drastically different timescales, ranging from minutes to days and years (e.g., Mauk et al., 2012). The NASA Van Allen Probes mission has collected radiation belt data with unrivaled quality and resolution over its seven years of continuous operation. This mission allowed for the most detailed and complete assessment of radiation belt dynamics to date, and has resulted in multiple ground-breaking discoveries (Reeves et al., 2013; Mann et al., 2013; Baker et al., 2014; Mann et al., 2016; Li et al., 2019, to list a few). However, assessing radiation belt dynamics on timescales shorter than the orbital period of the Van Allen Probes is challenging due to the lack of high spatio-temporal coverage of a rapidly evolving belt even with the twin Van Allen belt spacecraft.

In this paper, we analyze a geomagnetic storm that occurred on September 7-9, 2017, and was characterized by an extremely fast radiation belt dropout, following by a very fast and intense recovery ultimately associated with energization up to ∼10 MeV energies. In addition to explaining the radiation belt dynamics during this event, we show how utilizing the data from a single satellite mission, i.e, illustrated here using data from a single Van Van Allen Probe, can cause misinterpretation of the data during events with fast changes on sub-orbital timescales. Using a fortuitous spatial and temporal conjunction between the two Van Allen Probe spacecraft during a period of very fast acceleration, we are able to show here how an apparent local peak in electron phase space density (PSD) observed along the orbit of a single satellite is instead explained by the evolution of a monotonic PSD profile generated by fast inwards radial diffusion.

2 Overview of the September 2017 storm

The overview of the September 2017 storm shown in Figure 1 demonstrates that it was a relatively intense geomagnetic storm. It was associated with two periods of decreasing Dst, reaching -142 nT and then -124 nT separated by around 12 hours (cf. Figure 1 1(d)). Figure 1(a-c) show solar wind speed, interplanetary magnetic field (IMF),

and solar wind dynamic pressure throughout the storm. These plots reveal that the geomagnetic storm started on September 7, 2017, at around 00 UT with an intense increase in the solar wind speed and dynamic pressure and with the southward component of the IMF reaching a minimum of around -10 nT over the next several hours. At around 22 UT on September 7, the IMF turned very strongly southward, reaching the value of -31 nT by 24 UT. This period of strongly southward IMF is also associated with a secondary increase in solar wind speed and dynamic pressure. Finally, at around 12 UT on September 8, there is a secondary decrease in IMF B_z but no substantial changes in other solar wind parameters. Figure 1(d) shows the resulting Dst and Kp geomagnetic indices, that are consistent with the characteristics of the driving solar wind, marking the beginning of the storm with an increase in Dst on September 7, and with two subsequent geomagnetically active periods on September 8. Figure 1(e) shows the location of the last closed drift shell (LCDS), representative of the interaction of the LCDS with the magnetopause (cf., Olifer et al., 2018). The LCDS dynamics are relatively complex during this event, however, the most significant compressions of the LCDS occurred during the two IMF $B_z < 0$ periods on September 8, reaching L^* values as low as 3.9 and 4.3, respectively.

Figure 2 shows the Van Allen radiation belt response during the September 2017 event. In this study, we analyze radiation belt electron flux measurements from the Combined Xray Dosimeter (Morley et al., 2017, and references therein) on-board 21 Global Positioning System (GPS) satellites (Figure 2(a)), as well as from the Relativistic Electron Proton Telescope (REPT) instrument (Baker et al., 2012) on board of the two Van Allen Probes (Figure 2(b)). Both datasets show similar storm-time behavior of the trapped radiation, data from the constellation of GPS satellites revealing the electron dynamics with much higher spatio-temporal resolution than the Van Allen Probes (e.g., Olifer et al., 2018, and references therein). Figure 2(a) shows that the beginning of the storm on September 7 is followed by moderate loss at high L^*, and confinement of the radiation belt to $L^*<5.5$. Figure 2(b) shows evidence that the lower L^* in the heart of the radiation belt are being depleted to some degree at this time as well. The strong compression of the LCDS at around 0 UT on September 8 is associated with rapid and intense losses at L^* above the LCDS as revealed in the GPS data, and which are obvious in two subsequent passes of the Van Allen Probes data around that time. The recovery and the replenishment of the belt starts immediately after the loss at $\sim$3 UT on the same

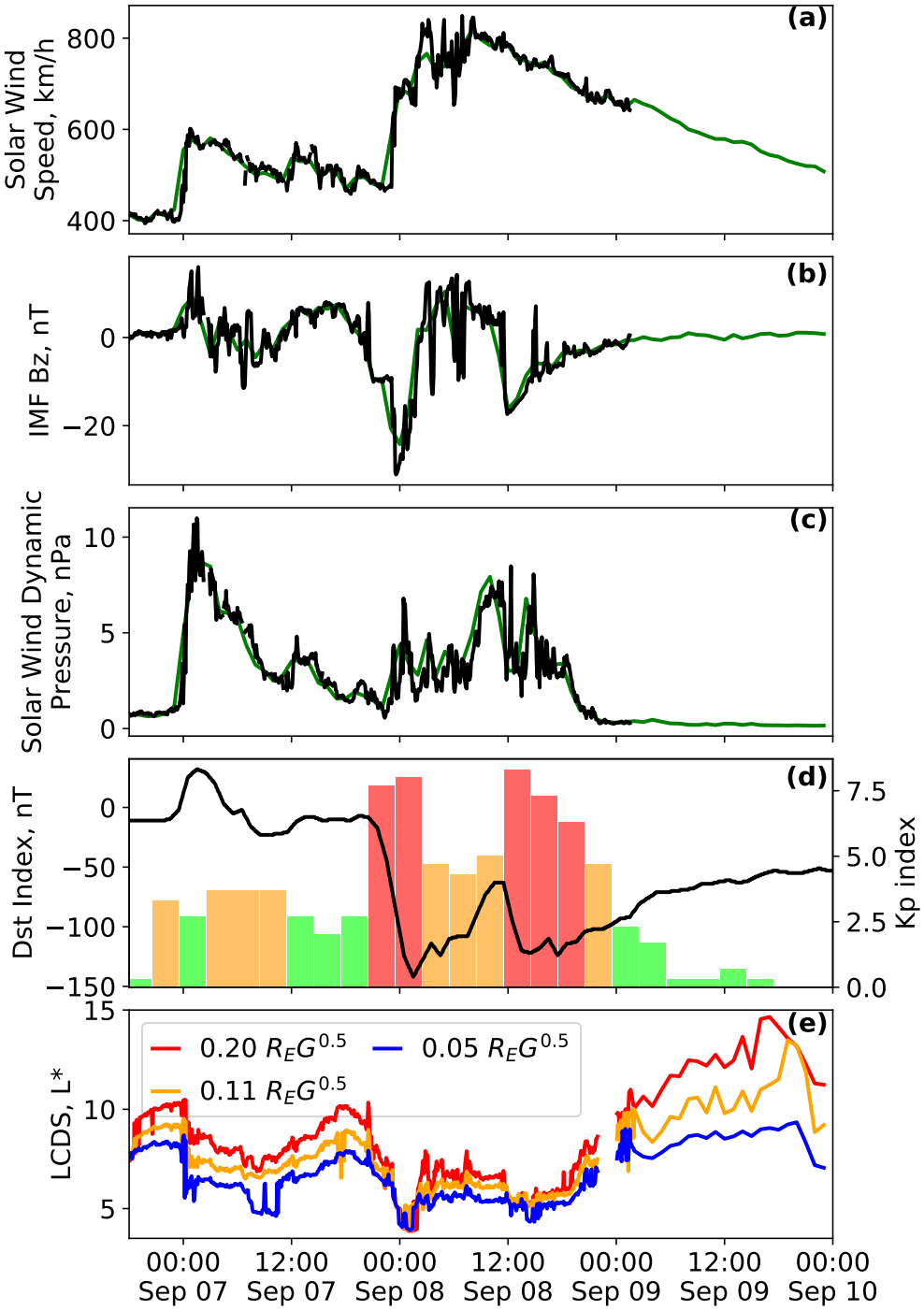

Figure 1. An overview of the September 7-9, 2017 geomagnetic storm. (a) solar wind speed, (b) B_z component of the interplanetary magnetic field, (c) solar wind dynamic pressure. Panels (a-c) show 5-min resolution solar wind data in black and 1-hr resolution data in green. High-resolution solar wind data is absent for the majority of September 9. (d) Dst index as a line plot and Kp index as a histogram (secondary y-axis). (e) Location of the last closed drift shell (LCDS) in L^* calculated for three different second adiabatic invariants, K shown in different colours defined in the legend using Tsyganenko and Sitnov (2005) geomagnetic model and the LANLGeoMag library (Henderson et al., 2017).

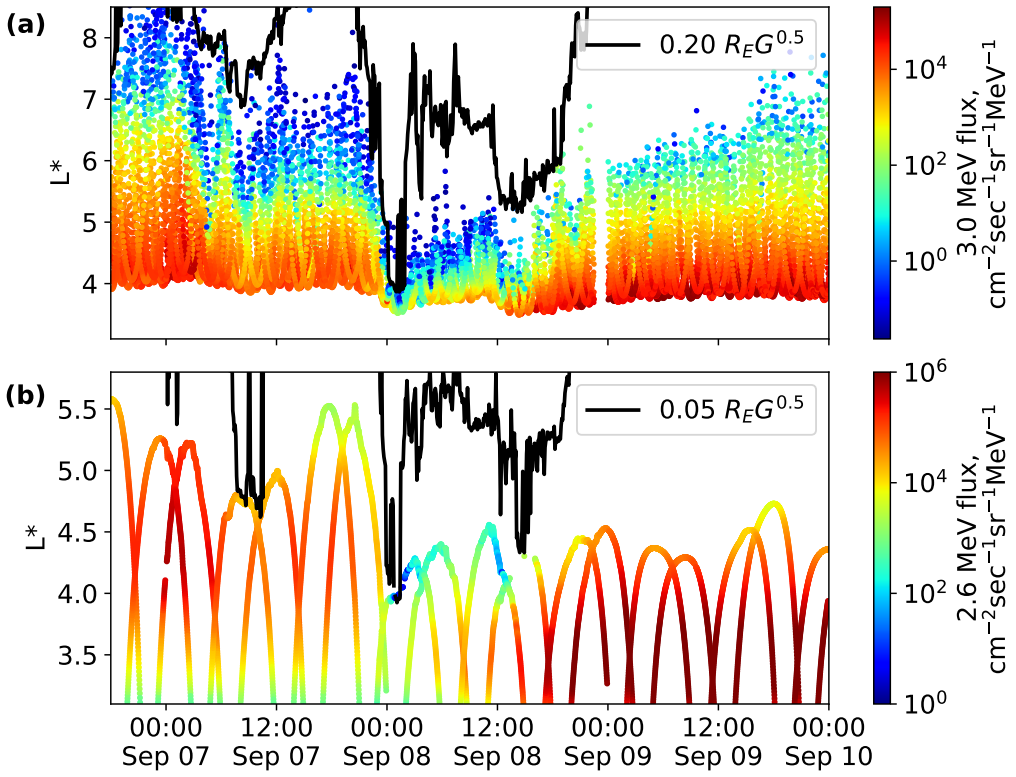

Figure 2. Radiation belt response during the September 7-9, 2017 geomagnetic storm. (a) 3 MeV electron flux measured by the constellation of Global Positioning System (GPS) satellites (Morley et al., 2017) as a function of time and L^*, overplotted with the last closed drift shell (LCDS) location in black. (b) 90° pitch angle 2.6 MeV electron flux measured by the Van Allen Probes (Baker et al., 2012) overplotted with the LCDS location. The Tsyganenko and Sitnov (2005) geomagnetic field model and LANLGeoMag library (Henderson et al., 2017) are used for calculation of the LCDS location and the L^* values for the satellites.

day. However, it is interrupted by a second geomagnetically active period that causes some of the newly recovered electron population at L^* around 4-5 to be lost. The recovery process continues uninterrupted until the radiation belt fluxes increase by an order of magnitude over the pre-storm levels.

3 Detailed analysis of radiation belt loss and recovery

To reveal the non-adiabatic effects of wave-particle interactions on the radiation belt electrons we analyze electron phase space density (PSD) over the course of the storm. The electron PSD is calculated using the algorithm (e.g., Morley et al., 2013) for con-

version between electron flux measurements and an estimate of electron PSD. The calculations were performed using the Tsyganenko and Sitnov (2005) magnetic field model, utilizing electron flux data from the combination of Magnetic Electron Ion Spectrometer (MagEIS) (Blake et al., 2013) and Relativistic Electron Proton Telescope (REPT) (Baker et al., 2012) particle detectors. Such an approach provides access to a wide energy range of electron flux measurements from ∼100 keV to ∼10 MeV and enabling the analysis of a wide range of first and second adiabatic invariants even at high L-shells. In addition, we used the magnetic field measurements from the Electric and Magnetic Field Instrument Suite and Integrated Science (EMFISIS) suite (Kletzing et al., 2013) to validate the Tsyganenko and Sitnov (2005) model used in the calculation of PSD and to calculate the first adiabatic invariant. To obtain the electron PSD as a function of the first adiabatic invariant, μ, we perform fitting of the measured electron energy spectrum by a kappa-distribution (Mauk & Fox, 2010), meanwhile, the dependence on the second adiabatic invariant, K, is obtained by linearly interpolating the observed pitch angle distributions to obtain the resolution required. Figure 3 shows the resulting electron PSD during the loss phase in panels (a, b) and the recovery phase in panels (c, d) for both Van Allen Probes A and B. Here, for the purposes of the detailed analysis which follows, we separate between the periods of dominant loss and recovery at 2:30 UT on September 8, 2017. This is the time when the GPS electron flux data is starting to show signs of recovery in the ultrarelativistic (>2 MeV) energy channels around L^* of 3.5.

3.1 Loss period

Figure 3 (panels a, b) show the PSD profiles as a function of L* observed during the in- and out-bound passes of the Van Allen Probes during the loss phase of the September 2017 geomagnetic storm. As shown earlier in terms of flux, there are two clear periods of strong and fast loss. The first period starts at ∼6 UT on September 7, 2017, during an initial compression of the LCDS. The electron PSD on both probes shows signs of loss. Significantly, there are signs of an outward PSD gradient developing at that time. The loss is more pronounced on high L, at L^*>5, where the PSD drops by more than an order of magnitude from the pre-storm levels. Meanwhile, in the heart of the radiation belt at L^*≈4.5 the radiation belt appears to be only depleted by a factor of around 2. This loss period is followed by a relatively stable period where the radiation belt morphology remains approximately constant, with little overall depletion or recovery, un-

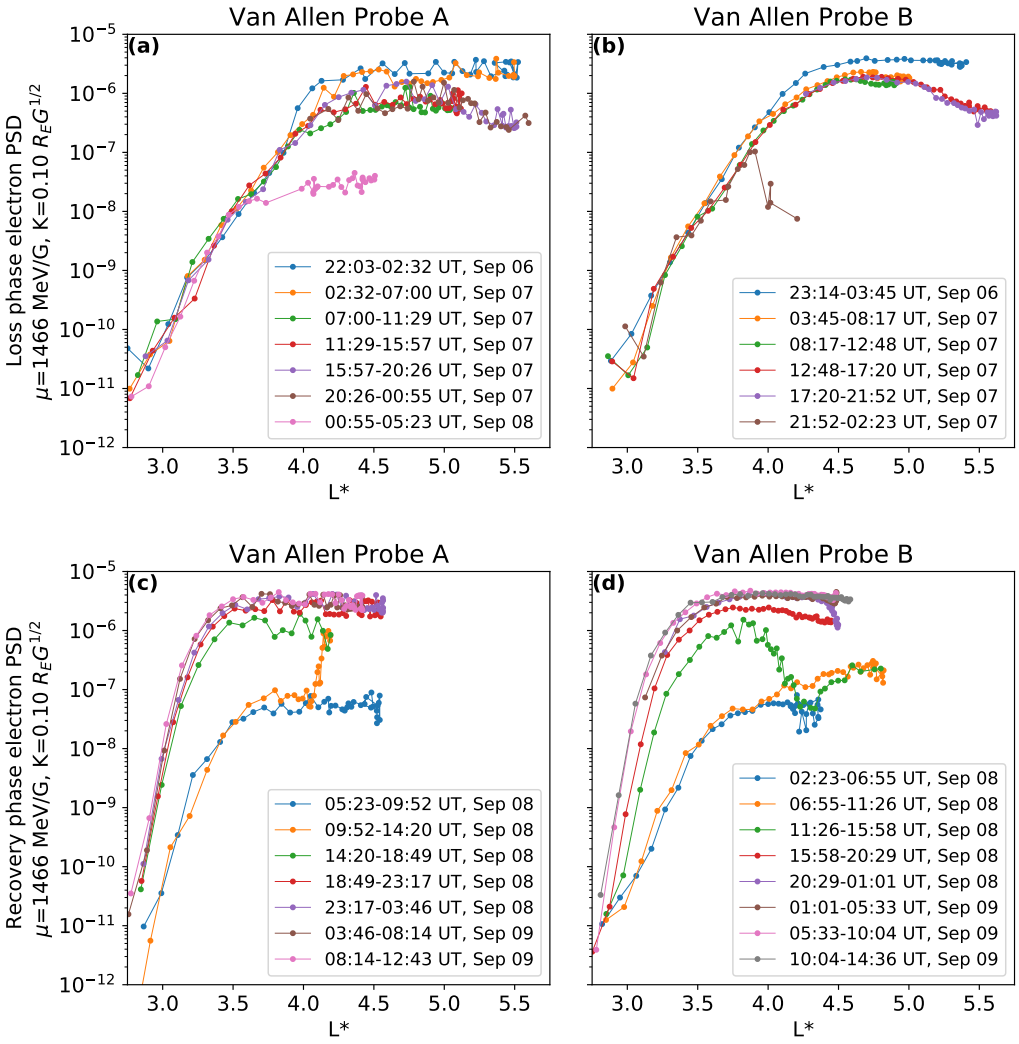

Figure 3. Electron phase space density (PSD) in units of $c^3 cm^{-3} MeV^{-3}$ during the September 7-9, 2017 geomagnetic storm. The data is shown as a function of L^*, for fixed first and second adiabatic invariants μ=1466 MeV/G and K=0.10 $R_E G^{1/2}$. PSD during the loss phase for Van Allen Probe A (panel a) and B (panel b). Different colors represent different inbound and outbound passes of the probes. PSD during the recovery phase for the Van Allen Probe A (panel c) and B (panel d). See text for details.

til 0 UT on September 8, 2017. At that time, the LCDS is rapidly compressed into the heart of the radiation belt, reaching L^*=3.9. This immediately depletes the electrons at higher L-shells and results in a further very rapid loss, which reaches L* of around 3.5, and which further depletes the PSD at L^* of around 4.5 by 2-3 orders of magnitude. Notably, the outbound pass of the Van Allen Probe B at 21:52-02:23 UT on September 7-8 (brown color in Figure 3b) shows that a steep outward gradient has developed along the depleted flux tubes above L^*=3.8. The subsequent pass of Van Allen Probe A at 00:55-05:23 UT on September 8 shows how this gradient is flattened by depletion of the PSD between L^* of 3.5 and 4.0. Such behavior of the radiation belt is consistent with losses caused by magnetopause shadowing and enhanced by outward radial diffusion. The timing of the losses, and the PSD profiles observed by Van Allen Probes A and B, occur at the time of the inwards motion of the LCDS, with the outwards PSD gradients further supportive of outwards radial diffusion inside the LCDS (e.g., Shprits, Elkington, et al., 2008; Mann et al., 2016; Ozeke et al., 2020).

The loss on September 8, 2017, is so intense that it depletes the radiation belt over the course of a single Van Allen Probe orbit. By contrast, however, the accompanying spatio-temporal dynamics are resolved in the combined data from the GPS satellite constellation (cf. Figure 2a). Overall, the large scale morphology of the radiation belts follows the dynamics of the LCDS. In this way, the results presented here are very similar to those reported by Olifer et al. (2018). Olifer et al. assessed the belt dynamics during 4 geomagnetic storms and demonstrated that the very fast and intense losses were associated very closely with the dynamics of the LCDS. Consistent with the conclusions of Olifer et al. (2018), the dynamics of the fast loss processes reported here also appear to be controlled by the dynamics of the envelope of the L^* of the LCDS and related magnetopause shadowing. Due to the speed of the loss processes which are operating, the results presented here again demonstrate the value and utility of using data from the constellation of GPS satellites to monitor and diagnose the resulting impacts on the belts.

3.2 Recovery and Acceleration Period

We now turn to examine the belt dynamics during the period of belt recovery and dominant acceleration starting around 02:30 UT on September 9, 2017. Unlike the dynamics resolved during the loss interval, the PSD data from the two Van Allen Probes (Figure 3, panels c and d) shows rather different behavior along the world-lines of the

in- and out-bound satellite orbits during this period of dominant acceleration. As we describe in detail below, the different profiles observed by Van Allen Probes A and B demonstrate that the belt morphology is changing very rapidly on the timescale of the satellite traversal through the outer belt. Moreover, a fortuitous conjunction in L^* and time provides the opportunity to resolve the spatio-temporal ambiguity thereby revealing important information about the active acceleration processes. The local peak in PSD seen by Probe B is confined to the L^* range between 3 and 4.25 and such features and belt morphology are usually considered to be suggestive of the signature of local acceleration processes, for example, connected to acceleration by VLF chorus waves. However, the observation of a narrow peak in L^* by one probe at the same time as the other probe reveals the increase of PSD at the outer boundary raises a question about the dominant acceleration processes which are active at this time. In particular, in the analysis presented below, we show how this apparent local peak in PSD can be explained by inward radial transport acting on timescales shorter than the orbital period of Van Allen Probes, therefore creating a spatio-temporal ambiguity in the PSD data as a function of L* and time.

Indeed, when combined, the PSD data from Van Allen Probes A and B during the most intense period of the enhancement phase (10-16 UT on September 8) reveal that the overall belt evolution is characterized by rapidly evolving inwards radial gradients, apparently driven by an external source. Figure 4 shows combined PSD data from both probes during the interval of close conjunction in L^*, at fixed first and second adiabatic invariants, μ and K. In each panel, data from the out-bound Probe A and the in-bound Probe B are shown in orange and pink, respectively. Data from passes immediately before and after the fast acceleration are shown as grey dots. The near-simultaneous electron population measurements allows a calculation of the direction of the PSD gradients during the enhancement phase, almost contemporaneously, provided that both probes are located inside the radiation belt with different values of L^*. These gradients are shown with three straight lines connecting data from the two Van Allen Probes at the same time, revealing the local direction of the PSD gradient at those times. Note that the profiles are only shown for the period from 13:00 UT until 13:20 UT, as at other times one of the probes is close to the magnetopause and the Tsyganenko and Sitnov (2005) magnetic field model fails to recreate the observed magnetic field at the satellite location, therefore preventing accurate analysis of the PSD as a function of L^* at fixed K. Refer to the

supplementary material for the comparison of the magnetic field measurements from the Van Allen Probes and estimating the location of the magnetopause using the THEMIS (Angelopoulos, 2008) satellites. Nonetheless, the analysis of the PSD dynamics is clear – there is an abrupt and very fast acceleration of the electrons with the instantaneous PSD gradients, and the PSD dynamics both inside and outside the probe conjunction region at $L^*{\sim}3.75$, indicative of acceleration which occurred as a result of fast inwards transport. In the next section, we use a ULF wave radial diffusion model to demonstrate clearly that inward ULF wave transport caused the rapid acceleration observed in the belt.

4 Recreating a local peak in electron PSD by inward radial diffusion

On account of the observed instantaneous inward PSD gradients, it is interesting to evaluate the ability of the radial diffusion to recreate the local peak in electron PSD observed in the Van Allen Probe B data. We perform a radial diffusion simulation using initial conditions from the observed pre-acceleration Van Allen probe flux (e.g., lower grey PSD profile in Figure 4), using radial diffusion coefficients from the Ozeke et al. (2014) Kp parametrization. The boundary conditions are shown in Supplementary Figure S4 and represent a short loss period, observed by Van Allen Probe B from 11:30 UT until 12:00 UT, which coincides with the inward motion of the LCDS, followed by a sharp assumed enhancement of the outer boundary electron population which acts as a source population for the subsequent inwards radial diffusion. Figure 5 shows the instantaneous PSD PSD profiles as a function of L^*, obtained from the radial diffusion simulation, as well as a PSD profile observed by a virtual spacecraft within the simulation domain and which is representative of Van Allen Probe B accounting for its orbital dynamics during the inbound pass. Note that that similar behavior is observed for electrons with different μ (cf. Figure 4), thus the simulation results in Figure 5 are representative of the relativistic electron population overall.

Figure 5 shows the overall temporal evolution of the electron PSD L^* profile inside the Van Allen radiation belt over the course of the event. PSD profiles during the short loss phase (11:30-12:00 UT) at the beginning of the Van Allen Probe B pass are shown in green-to-blue colors. This time coincides with the time of increased geomagnetic activity and a short compression of the LCDS (c.f., Figure 1). Figure 4 reveals the loss and a decreasing PSD as Probe B moves inbound from apogee. The same rapid drop

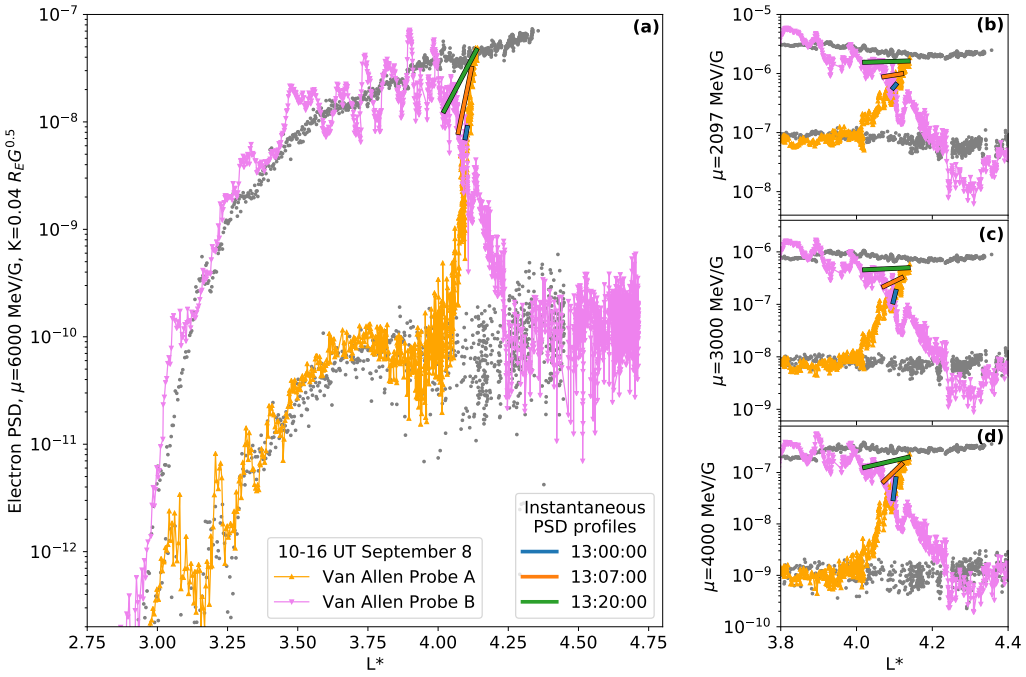

Figure 4. Van Allen Probe electron phase space density (PSD) in units of $c^3 cm^{-3} MeV^{-3}$ during the acceleration phase on September 8, 2017. (Panel a) Complete in-bound and out-bound passes of the Van Allen Probes for the population with μ=6000 MeV/G and K=0.04 $R_E G^{0.5}$. At the time of the conjunction, at L^*=4.0, this corresponds to electron energy of 2.5 MeV and 75° pitch angle. The data from the two Van Allen Probe passes during the period of the acceleration are shown in orange (Probe A, outward pass) and pink (Probe B, inward pass) colors. The PSD profiles immediately before and immediately after the acceleration are shown in grey scatter plots. Instantaneous local PSD gradients are assessed using data from close to the orbital crossing point in L^* using 20 minutes of data from 13:00 to 13:20 UT, with the instantaneous data from the two probes being connected by short solid lines. (Panels b,c and d) PSD profiles as a function of L^* for three different μ values and fixed K=0.04 $R_E G^{0.5}$, in the region of the narrow L^* crossing regions between L^*=3.8 and L^*=4.4, shown in the same format as panel (a).

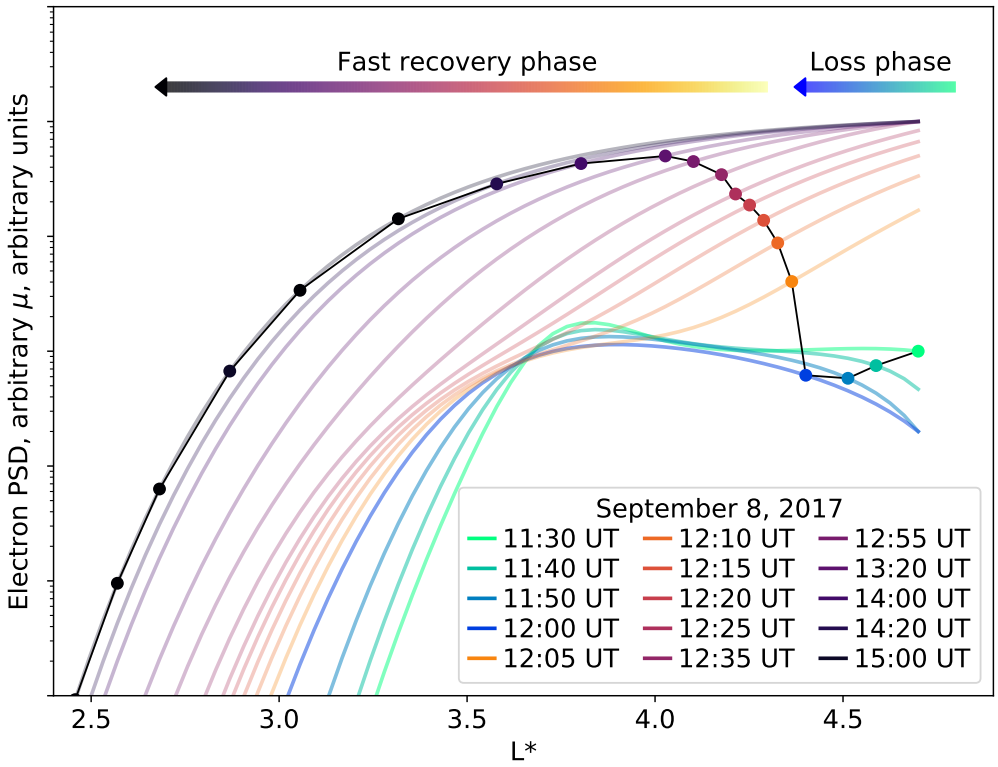

Figure 5. Electron phase space density (PSD) profiles as a function of L^* obtained from the radial diffusion simulation of the acceleration phase during September 8, 2017, with measurements from the inbound pass of a virtual Probe B through the simulation shown in solid circles. The instantaneous PSD profiles across the full L^* range derived from the radial diffusion model are shown in two sets of colors: green-to-blue during the short loss phase and yellow-to-purple during the acceleration phase. The solid colored dots with connected black lines represents a recreation of the Van Allen Probe B data during an inbound pass of a virtual satellite, after tracing the temporal L^* trajectory of the satellite. This simulation shows how fast inward radial diffusion can can create apparent local peaks in PSD in the frame of the satellite, especially when the belt is evolving on timescales faster than the orbital period of the satellite.

in PSD is recreated in Figure 5, showing that the inward PSD gradient at L^*>4.25, revealed by Van Allen Probe B, is consistent with outward radial diffusion and magnetopause shadowing. This short loss phase is followed by an intense and rapid acceleration (post 12:00 UT). Figure 5 shows the radial PSD profiles during this time in yellow-to-orange-to-purple colors. While the PSD gradients for instantaneous L^* profiles remain directed inward, the orbital movement of Probe B causes it to observe an apparent local L^* peak while the satellite continues its inbound pass and observes levels of PSD which are still increasing. The key point here is that when the belts are evolving under the action of fast acceleration processes, the observation of a local L^* peak in PSD should not necessarily be automatically associated with a local acceleration process. Indeed, in the example presented here a fortuitous temporal and L^* conjunction between Van Allen Probes A and B reveals that the local L^* peak in PSD is instead generated by the inward motion of the satellite through rising but monotonic PSD L^* profiles as a result of fast inward radial diffusion. Notably and as discussed by Mann and Ozeke (2016) (see also Mann et al., 2016), ULF wave radial diffusion can be responsible for the inward radial transport of Van Allen belt elections from a source population at the outer edge into the heart of the belt on timescales much faster than is often thought. As we show here, this can occur on sufficiently short timescales that it complicates the analysis of PSD profiles observed along the world-line of single satellites in geosynchronous transfer orbits.

5 Conclusions

Overall, our findings when analyzing the loss and acceleration of Van Allen radiation belt electrons during the intense geomagnetic storm on September 7-9, 2017 can be summarized by the following points:

1. The fast loss of relativistic and ultra-relativistic electron populations is observed during the September 2017 storm in electron flux data measurements from the constellation of 21 GPS satellites and from the dual spacecraft of the NASA Van Allen Probes mission. Analysis of the electron phase space density (PSD) and high temporal resolution dynamics of the last closed drift shell (LCDS) demonstrates that the observed fast losses can be explained by magnetopause shadowing losses enhanced by outward radial diffusion.
2. An apparent local L^* peak in PSD is observed during the subsequent in-bound pass of Van Allen Probe B during the storm acceleration phase. However, an out-

bound pass of Van Allen Probe A, at the same time and in conjunction with Probe B, observed a totally different PSD profile as a function of L^* being characterized by an inward gradient. A combination of the Van Allen Probes A and B PSD data reveals instantaneous PSD profiles with inward gradients, suggestive of the action of fast inward radial diffusion.

3. A radial diffusion simulation of the acceleration phase during the September 2017 storm shows that the local peak in PSD, observed in the Van Allen Probe B data, is an artifact of the spatio-temporal evolution of the radiation belt, combined with a relatively long orbital period of the satellite. In general, the result reported here highlights the importance of multi-point measurements for resolving the spatio-temporal ambiguities in fast belt dynamics. Indeed, and as shown here, an apparent local peak in PSD as a function of L^* can be created along an in-bound orbit even during periods of dominant inwards radial diffusion.
4. In general, our study shows that the observation of a single local peak in PSD cannot be used to definitively identify that local acceleration was the cause of the observed radiation belt enhancement, especially during periods of very fast dynamics. Instead, it can be the product of the inward radial diffusion and the analysis of periods of fast belt dynamics should be handled with care. Overall, and in the absence of other indicators, observations of local peaks in PSD as a function of L^* in single satellite data should not in and of themselves be used to infer the action of local acceleration processes. Careful analysis of ideally multi-point data, together with appropriate modeling, are in our view required when seeking to definitively identify the causative physical processes operating during fast radiation belt enhancements.

Acknowledgments

This work is partially supported by Canadian NSERC, and by the Canadian Space Agency through the Geospace Observatory Canada program. Contributions by SKM were performed under the auspices of the U.S. Department of Energy, with partial support from the Laboratory Directed Research and Development (LDRD) program, awards 20150127ER and 20190262ER. We gratefully acknowledge the CXD team at Los Alamos National Laboratory, which designed and built the CXD instrument discussed in this paper. The authors thank Harlan Spence and the ECT team for the Van Allen Probe data. Process-

ing and analysis of the REPT data was supported by Energetic Particle, Composition, and Thermal Plasma (RBSP-ECT) investigation funded under NASA's Prime contract no. NAS5-01072. All RBSP-ECT data are publicly available at the Web site `http://www.RBSP-ect.lanl.gov/`. The LANL-GPS particle data available through NOAA NCEI, at `http://www.ngdc.noaa.gov/stp/space-weather/s` Solar wind data, geomagnetic indices, and parameters for TS04 model are obtained from Tsyganenko model web page `http://geo.phys.spbu.ru/ tsyganenko/modeling.html`. The LANLGeoMag software library is available at `https://www.github.com/drsteve/LANLGeoMag`.

References

Angelopoulos, V. (2008, apr). The THEMIS Mission. *Space Science Reviews*, *141*(1-4), 5–34. Retrieved from `https://doi.org/10.1007%2Fs11214-008-9336-1` doi: 10.1007/s11214-008-9336-1

Baker, D. N., Jaynes, A. N., Hoxie, V. C., Thorne, R. M., Foster, J. C., Li, X., ... Lanzerotti, L. J. (2014, nov). An impenetrable barrier to ultrarelativistic electrons in the Van Allen radiation belts. *Nature*, *515*(7528), 531–534. Retrieved from `https://doi.org/10.1038%2Fnature13956` doi: 10.1038/nature13956

Baker, D. N., Kanekal, S. G., Hoxie, V. C., Batiste, S., Bolton, M., Li, X., ... Friedel, R. (2012, dec). The Relativistic Electron-Proton Telescope (REPT) Instrument on Board the Radiation Belt Storm Probes (RBSP) Spacecraft: Characterization of Earth's Radiation Belt High-Energy Particle Populations. *Space Science Reviews*, *179*(1-4), 337–381. Retrieved from `https://doi.org/10.1007%2Fs11214-012-9950-9` doi: 10.1007/s11214-012-9950-9

Blake, J. B., Carranza, P. A., Claudepierre, S. G., Clemmons, J. H., Crain, W. R., Dotan, Y., ... Zakrzewski, M. P. (2013, jun). The Magnetic Electron Ion Spectrometer (MagEIS) Instruments Aboard the Radiation Belt Storm Probes (RBSP) Spacecraft. *Space Science Reviews*, *179*(1-4), 383–421. Retrieved from `https://doi.org/10.1007%2Fs11214-013-9991-8` doi: 10.1007/s11214-013-9991-8

Henderson, M., Morley, S., Niehof, J., & Larsen, B. (2017, Dec). drsteve/LANLGeoMag: LANLGeoMag v.1.5.15-alpha. doi: 10.5281/zenodo.1133782

Kletzing, C. A., Kurth, W. S., Acuna, M., MacDowall, R. J., Torbert, R. B., Averkamp, T., ... Tyler, J. (2013, jun). The Electric and Magnetic Field

Instrument Suite and Integrated Science (EMFISIS) on RBSP. *Space Science Reviews*, *179*(1-4), 127–181. Retrieved from https://doi.org/10.1007%2Fs11214-013-9993-6 doi: 10.1007/s11214-013-9993-6

Li, J., Bortnik, J., An, X., Li, W., Angelopoulos, V., Thorne, R. M., ... Baker, D. N. (2019, oct). Origin of two-band chorus in the radiation belt of Earth. *Nature Communications*, *10*(1). Retrieved from https://doi.org/10.1038%2Fs41467-019-12561-3 doi: 10.1038/s41467-019-12561-3

Mann, I. R., Lee, E. A., Claudepierre, S. G., Fennell, J. F., Degeling, A., Rae, I. J., ... Honary, F. (2013, nov). Discovery of the action of a geophysical synchrotron in the Earth's Van Allen radiation belts. *Nature Communications*, *4*(1). Retrieved from https://doi.org/10.1038%2Fncomms3795 doi: 10.1038/ncomms3795

Mann, I. R., & Ozeke, L. G. (2016, jun). How quickly, how deeply, and how strongly can dynamical outer boundary conditions impact Van Allen radiation belt morphology? *Journal of Geophysical Research: Space Physics*, *121*(6), 5553–5558. Retrieved from https://doi.org/10.1002%2F2016ja022647 doi: 10.1002/2016ja022647

Mann, I. R., Ozeke, L. G., Murphy, K. R., Claudepierre, S. G., Turner, D. L., Baker, D. N., ... Honary, F. (2016, jun). Explaining the dynamics of the ultra-relativistic third Van Allen radiation belt. *Nature Physics*, *12*(10), 978–983. Retrieved from https://doi.org/10.1038%2Fnphys3799 doi: 10.1038/nphys3799

Mauk, B. H., & Fox, N. J. (2010, dec). Electron radiation belts of the solar system. *Journal of Geophysical Research: Space Physics*, *115*(A12), n/a–n/a. Retrieved from https://doi.org/10.1029%2F2010ja015660 doi: 10.1029/2010ja015660

Mauk, B. H., Fox, N. J., Kanekal, S. G., Kessel, R. L., Sibeck, D. G., & Ukhorskiy, A. (2012, sep). Science Objectives and Rationale for the Radiation Belt Storm Probes Mission. *Space Science Reviews*, *179*(1-4), 3–27. Retrieved from https://doi.org/10.1007%2Fs11214-012-9908-y doi: 10.1007/s11214-012-9908-y

Millan, R., & Thorne, R. (2007). Review of radiation belt relativistic electron losses. *Journal of Atmospheric and Solar-Terrestrial Physics*, *69*(3), 362 -

377. Retrieved from http://www.sciencedirect.com/science/article/pii/S1364682606002768 doi: https://doi.org/10.1016/j.jastp.2006.06.019

Morley, S. K., Henderson, M. G., Reeves, G. D., Friedel, R. H. W., & Baker, D. N. (2013, sep). Phase Space Density matching of relativistic electrons using the Van Allen Probes: REPT results. *Geophysical Research Letters*, *40*(18), 4798–4802. Retrieved from https://doi.org/10.1002%2Fgrl.50909 doi: 10.1002/grl.50909

Morley, S. K., Sullivan, J. P., Carver, M. R., Kippen, R. M., Friedel, R. H. W., Reeves, G. D., & Henderson, M. G. (2017, feb). Energetic Particle Data From the Global Positioning System Constellation. *Space Weather*, *15*(2), 283–289. Retrieved from https://doi.org/10.1002%2F2017sw001604 doi: 10.1002/2017sw001604

Olifer, L., Mann, I. R., Morley, S. K., Ozeke, L. G., & Choi, D. (2018, may). On the Role of Last Closed Drift Shell Dynamics in Driving Fast Losses and Van Allen Radiation Belt Extinction. *Journal of Geophysical Research: Space Physics*, *123*(5), 3692–3703. Retrieved from https://doi.org/10.1029%2F2018ja025190 doi: 10.1029/2018ja025190

Ozeke, L. G., Mann, I. R., Murphy, K. R., Rae, I. J., & Milling, D. K. (2014, mar). Analytic expressions for ULF wave radiation belt radial diffusion coefficients. *Journal of Geophysical Research: Space Physics*, *119*(3), 1587–1605. Retrieved from https://doi.org/10.1002%2F2013ja019204 doi: 10.1002/2013ja019204

Ozeke, L. G., Mann, I. R., Olifer, L., Dufresne, K. Y., Morley, S. K., Claudepierre, S. G., ... Degeling, A. W. (2020, feb). Rapid Outer Radiation Belt Flux Dropouts and Fast Acceleration During the March 2015 and 2013 Storms: The Role of Ultra-Low Frequency Wave Transport From a Dynamic Outer Boundary. *Journal of Geophysical Research: Space Physics*, *125*(2). Retrieved from https://doi.org/10.1029%2F2019ja027179 doi: 10.1029/2019ja027179

Reeves, G. D., Spence, H. E., Henderson, M. G., Morley, S. K., Friedel, R. H. W., Funsten, H. O., ... Niehof, J. T. (2013, jul). Electron Acceleration in the Heart of the Van Allen Radiation Belts. *Science*, *341*(6149), 991–994. Retrieved from https://doi.org/10.1126%2Fscience.1237743 doi: 10.1126/science.1237743

Shprits, Y. Y., Elkington, S. R., Meredith, N. P., & Subbotin, D. A. (2008, nov). Review of modeling of losses and sources of relativistic electrons in the outer radiation belt I: Radial transport. *Journal of Atmospheric and Solar-Terrestrial Physics*, *70*(14), 1679–1693. Retrieved from https://doi.org/10.1016%2Fj.jastp.2008.06.008 doi: 10.1016/j.jastp.2008.06.008

Shprits, Y. Y., Subbotin, D. A., Meredith, N. P., & Elkington, S. R. (2008, nov). Review of modeling of losses and sources of relativistic electrons in the outer radiation belt II: Local acceleration and loss. *Journal of Atmospheric and Solar-Terrestrial Physics*, *70*(14), 1694–1713. Retrieved from https://doi.org/10.1016%2Fj.jastp.2008.06.014 doi: 10.1016/j.jastp.2008.06.014

Tsyganenko, N. A., & Sitnov, M. I. (2005). Modeling the dynamics of the inner magnetosphere during strong geomagnetic storms. *Journal of Geophysical Research*, *110*(A3). Retrieved from https://doi.org/10.1029%2F2004ja010798 doi: 10.1029/2004ja010798

Van Allen, J. A., & Frank, L. A. (1959, feb). Radiation Around the Earth to a Radial Distance of 107,400 km. *Nature*, *183*(4659), 430–434. Retrieved from https://doi.org/10.1038%2F183430a0 doi: 10.1038/183430a0